



Science Arts & Métiers (SAM)

is an open access repository that collects the work of Arts et Métiers Institute of Technology researchers and makes it freely available over the web where possible.

This is an author-deposited version published in: <https://sam.ensam.eu>
Handle ID: <http://hdl.handle.net/10985/12175>

To cite this version :

Patrice PEYRE, Sébastien POUZET, Olivier CASTELNAU, Morgan DAL - Simplified numerical model for the laser metal deposition additive manufacturing process - Journal of Laser Applications - Vol. 29, n°2, p.Article number 022304 - 2017

Any correspondence concerning this service should be sent to the repository

Administrator : scienceouverte@ensam.eu



Simplified numerical model for the laser metal deposition additive manufacturing process

Patrice Peyre, Morgan Dal, Sébastien Pouzet, and Olivier Castelnaud

PIMM Laboratory, UMR 8006 Arts et Métiers–CNRS–CNAM, 151 Bd de l'Hôpital, 75013 Paris, France

The laser metal deposition (LMD) laser technique is a free-form metal deposition process, which allows generating near net-shape structures through the interaction of a powder stream and a laser beam. A simplified numerical model was carried out to predict layer heights together with temperature distributions induced by the (LMD) process on a titanium alloy, and a metal matrix composite. Compared with previously developed models, this simplified approach uses an arbitrary Lagrangian Eulerian free surface motion directly dependent on the powder mass feed rate D_m . Considering thin wall builds of Ti-6Al-4V titanium alloy, numerical results obtained with COMSOL 4.3 Multiphysics software were successfully compared with the experimental data such as geometrical properties of manufactured walls, fast camera molten pools measurements, and thermocouple temperature recordings in the substrate during the manufacturing of up to 10 LMD. Even if the model did not consider coupled hydraulic-thermal aspects, it provides a more realistic local geometrical description of additive layer manufacturing walls than simpler thermal models, with much shorter calculation times than more sophisticated approaches considering thermocapillary fluid flow. In a second step, microstructures (equiaxed or columnar) were predicted on Ti-6Al-4V walls using microstructural map available in the literature, and local thermal gradients G (K/m) and solidification rate R (m/s) provided by the FE calculation near the solidification front.

Key words: LMD, Laser, modeling, titanium, additive manufacturing

I. INTRODUCTION

The direct laser metal deposition (LMD) or laser engineering net shaping (LENS) process allows to fabricate bulk materials from CAD drawings by a sequence of layer depositions involving laser melting–solidification of powder stream.^{1,2} Compared with powder bed techniques, it allows a much better addition rate but with: (1) a lower degree of complexity due to the melt-pool (MP) sizes (in the mm range for LMD and 0.1 mm range for laser metal fusion (LMF) and (2) higher roughness due to a factor of ten difference in layer thickness (around 50 μm for LMF process and 500 μm for LMD). The applications of LMD process also include refurbishing–repairing of damaged parts like titanium blades. More precisely, during an LMD process, a laser irradiation creates a molten region on the surface of a substrate. A stream of metal powders is fed into the laser-induced melt pool to form a layer and raise the global volume. The next layer is then built on the previous one, resulting in a 3D part (Fig. 1). Compared with powder bed additive layer manufacturing (ALM) techniques (LMF, electron beam melting (EBM)), manufactured structures exhibit a lower degree of complexity but the process allows building or repairing larger structures (up to 1 m), composite materials^{3,4} or graded materials, by a step-by-step change of feeding powder.

A clear and global physical understanding of the LMD process is complex as a whole because it addresses various aspects such as: (1) the laser–powder stream interaction; (2) the

laser-induced melt-pool-powder stream interaction, and the resulting geometry of parts; (3) the 3D thermal fields induced and the metallurgical and mechanical modifications.

Many analytical or numerical studies have already addressed the different aspects of LMD, with more or less complex approaches.

Among the number of published studies, the analytical model proposed by Qi *et al.*² is still a valid and interesting piece of work to estimate the powder stream–laser interaction and predict the laser heating of powder by the laser beam for various process parameters (interaction distance, laser power, grain diameter). Similarly, Huang *et al.*¹ computed the attenuation of laser power by a powder stream, and the resulting temperature distribution of powder particles reaching the workpiece surface.

Various numerical or analytical models have also addressed the formation of wall geometries by considering either element activation including a time discretization of the process,^{5,6} predefined analytical function of the final shape like those by Pinkerton and Li⁷ or Fathi *et al.*,⁸ or a more physical self-consistent displacement of the free surface including the powder feed distribution in the velocity^{2,9,10} with the use of a level-set method.

However, except in Ref. 5, most of these works did not consider multilayer formation. Moreover, excessive calculation times are the main reason why most of these works did not include the calculation of thermally assisted fluid flow, which are known to play a dominant role in the final shaping

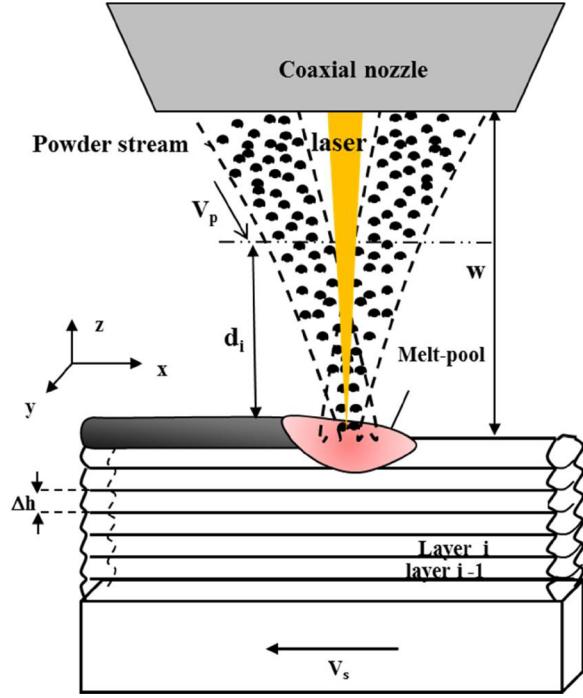


FIG. 1. Basic principle of the LMD process.

of molten + solidified walls. Morville *et al.*^{11,12} proposed a thermohydraulic complex 2D and 3D models taking into account the solid + fluid coupling, and considering the Marangoni flow. In the 3D model¹² as indicated above, this multiphysic modeling was limited to the first additive layer, due to prohibitive calculation times.

In all the previously mentioned works, the free surface evolution during deposition was considered either with a level-set function^{1,9,13} tracking the gas–solid interface or with an Arbitrary Lagrangian Eulerian (ALE) procedure.^{11,12}

Last, recent modeling like those by Mirzade¹³ have considered undercooling during crystallization as a possible modification of melt zone contours whereas Suarez *et al.*¹⁴ have considered metallurgical phase transformation of Ti-6Al-4V during LMD, following previous works by Kobryn *et al.* who established microstructure maps.¹⁵

In our recent work, different FE models were proposed, starting from rather simple solid simulations considering layer growth through the x-displacement of a thermal conductivity front (Heaviside step function)¹⁶ on predefined layers. The main drawback of this model was the heat source positioning (on the top of planar additive layers) which was not fully representative of the real laser absorption on an inclined shape.

Following these numerical works, widely reported in a recent literature review by Thompson,¹⁰ our objective was to develop a numerical solid thermal + morphological approach, with the main objective to provide a precise description of laser-induced melt-pool shapes in order to predict both wall geometries (layer heights) and thermal fields, and to validate it with dedicated experimental diagnostics. An important point to notice is that the fluid flow was not assumed in order to ensure affordable calculation times.

The main input parameters for the model were: the mass feed rate D_m (g/min), the laser power distribution Φ (W/m^2) = $f(x,y)$, and the scanning speed V (m/s), and the time delay Δt between subsequent layers, equal to 10 s. The only adjustable parameter was the laser absorption coefficient A . The model was confronted to experimental data (melt-pool geometries, thermocouple temperature data) recorded during the LMD process applied on a Ti-6Al-4V titanium alloy. Compared with previous works, the real novelty of this work is to provide a simple but robust numerical thermometallurgical model supported by dedicated experimental validations.

II. NUMERICAL AND EXPERIMENTAL CONDITIONS

A. The numerical ALE model

The finite element model, implemented in COMSOL 4.3 MultiphysicsTM solves heat equation in transient conditions (Eq. (1)), considering a solid state, i.e., without addressing fluid flow and solving Navier Stokes equations. Up to ten additive layers were considered in the current work, but the model in itself should be valid for much longer building times. Nonlinear thermophysical properties of Ti-6Al-4V were used, and the enthalpy of fusion L_f was considered as a modification of the specific heat C_p^{eq} (Eq. (2))

$$\rho(T)C_p^{eq}(T)\frac{\partial T}{\partial t} = \vec{\nabla} \cdot (\lambda(T)\vec{\nabla}T) \quad (1)$$

$$C_p^{eq}(T) = C_p(T) + L_m D_m(T)$$

$$\text{with } D_m(T) = \frac{1}{\sqrt{\pi}\Delta T^2} \cdot \exp\left(-\frac{(T - T_m^2)}{\Delta T^2}\right) \quad (2)$$

1. Boundary conditions

The starting geometrical model is composed of a $62 \times 10 \times 1$ mm substrate with a (O, x, z) symmetry plane, and a continuous heat flux condition applied on its bottom part, including radiative and convective losses (Eq. (3)). Due to the symmetry plane, less than half of the real substrate (a 2-mm-width plate) was considered. The model was mostly based upon the free surface motion of the upper building surface in the $(0,z)$ direction, and at a velocity V_z . At first, an attempt was made to apply normal velocity exclusively above the melting point of the built material, which is physically consistent with the real experimental conditions of layer growth during LMD. However, due to the nonuniform dimensions of the melt-pool, this condition was shown to induce excessive deformation of the wall central axis where the melt-pool is longer. Moreover, a realistic spatial distribution, $V_z = f(x;y)$, was used (Eq. (4)), in order to represent additive layer geometries (Fig. 2), even if they are more dependent on gravity forces and surface tension applied on MP than on powder feed distribution. Consequently, V_z was represented as a spatially uniform value dependent on the mass feed rate. However, as shown in Ref. 18, for usual mass feeding conditions (Gaussian distribution), efficient mass feed rates $D_{m,eff}^*$ (kg/s), dependent on MP size, have to be used to represent correctly matter addition. For all these

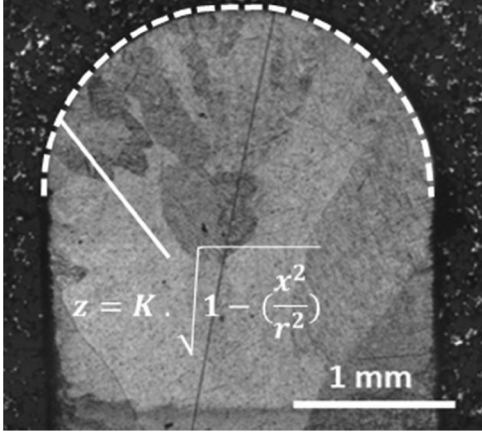


FIG. 2. Cross-section of an LMD wall including the last layer semicircular shape.

reasons, a simplified formulation of V_z has been used (Eq. (4)). For our experimental conditions ($D_m = 2.5$ g/min), a $V_{z,0}$ value near 0.0015 m/s was calculated and applied to the upper building surface

$$-\lambda(T) \frac{\partial T}{\partial n} = \varnothing_0 - h_c(T - T_{\text{inf}}) - \varepsilon\sigma(T^4 - T_{\text{inf}}^4)$$

with $\varnothing_0 = \frac{A \cdot P_0}{\pi r_0^2}$ (3)

$$V_z = V_{z,0} \cdot \sqrt{1 - \left(\frac{x^2}{rp^2} + \frac{y^2}{rp^2} \right)}$$

with $V_{z,0} = \frac{D_{m,\text{eff},*}}{\rho \cdot \pi \cdot rp^2}$

for $(X^2 + Y^2) < rp^2$ and $X = X_0 - V_0 \cdot t$ (4)

2. Mesh optimization

The use of an ALE method for addressing surface displacements, which tends to elongate mesh elements in the (O - z) direction, is mostly constrained by a balance between sufficiently fine elements to provide a valid and spatially well resolved calculation of temperature fields, but not too fine elements to limit excessive vertical deformation during layer addition. In the optimized model presented in Fig. 3,

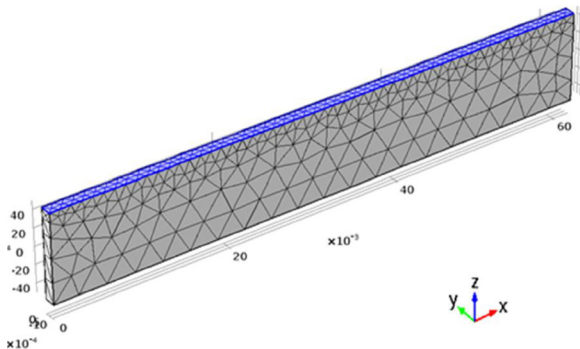


FIG. 3. Starting LMD model (1256 elements). A V_z velocity boundary condition is applied on the blue surface.

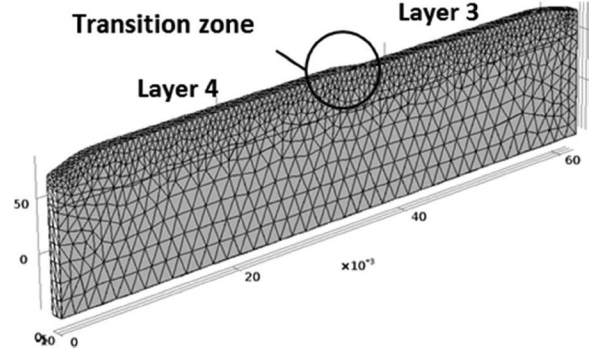


FIG. 4. Remeshed model during the fifth LMD layer at 0.4 m/min.

the aspect ratio of surface elements was shrunk along (O , z) to anticipate further deformation during ALM. A size condition (maximum tolerated size of 0.35 mm) was also applied to the upper face to provide a sufficiently high number of elements inside calculated fusion isotherms of melt-pools. For the optimized starting condition, 1256 tetrahedral elements were used, and a remeshing condition was applied to the initial model (Fig. 4).

B. LMD conditions and associated diagnostics

LMD tests were carried out using Ti6Al4V powders (45–75 μm range) on an industrial Optomec 850 LENS machine and on an opened LMD setup with various diagnostics around the laser-powder stream-melt-pool interaction zone. Two laser powers P_0 (400 W and 600 W) with a top-hat beam distribution ($D_0 = 1.7$ mm) and two scanning speeds V_s were used (0.2 and 0.4 m/min), for a constant mass feed rate of $D_m = 2.5$ g/min, and a time pause $\Delta t = 10$ s applied between subsequent layers to stabilize layer growth. Such conditions correspond to different energy densities E (J/mm^2) where E (J/mm^2) = $(4 P_q)/(V_s (\pi D_0))$, ranging between 45 J/mm^2 (P400 V400) and 134 J/mm^2 (P600 V200). All the tests were carried out in a refurbishing configuration, i.e., starting from a thin Ti-6Al-4V substrate of 2 mm width. For such conditions, layer heights were comprised between 0.6 and 0.7 mm (for $V_0 = 0.4$ m/min) and 1–1.1 mm (for $V_0 = 0.2$ m/min), which is in good agreement with the powder accumulation time in the melt-pool (function of V_0^{-1}).¹⁶ It also can be noticed that laser power P_0 has a limited influence on layer height, but mostly tends to reduce A_h , due to a reduction of efficient mass feeding for increased layer widths—Table I).

TABLE I. LMD conditions and wall geometries (width e , layer height A_h , MP length L , MP height H).

P400 V400	P400 V200	P600 V400	P600 V200
$P_0 = 400$ W	400 W	600 W	600 W
$V_s = 0.4$ m/min	0.2 m/min	0.4 m/min	0.2 m/min
$e = 2.1$ mm	2.5 mm	2.6 mm	3.3 mm
$\Delta h = 0.7$ mm	1.08 mm	0.6 mm	0.92 mm
$L = 2.4$ mm	3.3 mm	3.75 mm	4.2 mm
$H = 1$ mm	1.5 mm	1.25 mm	1.75 mm

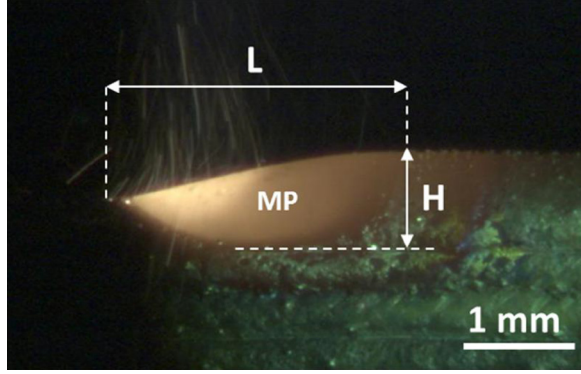


FIG. 5. Fast camera analysis of melt-pool (MP) size (P400V400).

A fast camera (Photron SA3, C-Mos sensor), operating between 2000 and 4000 Hz, was installed near the laser head to provide a real time lateral analysis (Fig. 5) of melt-pool (MP) size and dynamics.¹⁷

The change in MP size (length L and height H) with process conditions was used as a reliable data to validate the FE thermomorphological model. Type K thermocouples (0.125 mm width) were also installed (by electrodischarge spot welding) on the substrates before LMD to obtain thermal cycles $T=f(t)$ at specific locations (x_0, z_0) . A distance of 1.5–3 mm between the position of thermocouples and the top of the substrate (bottom of the first additive layer) was selected for all LMD tests.

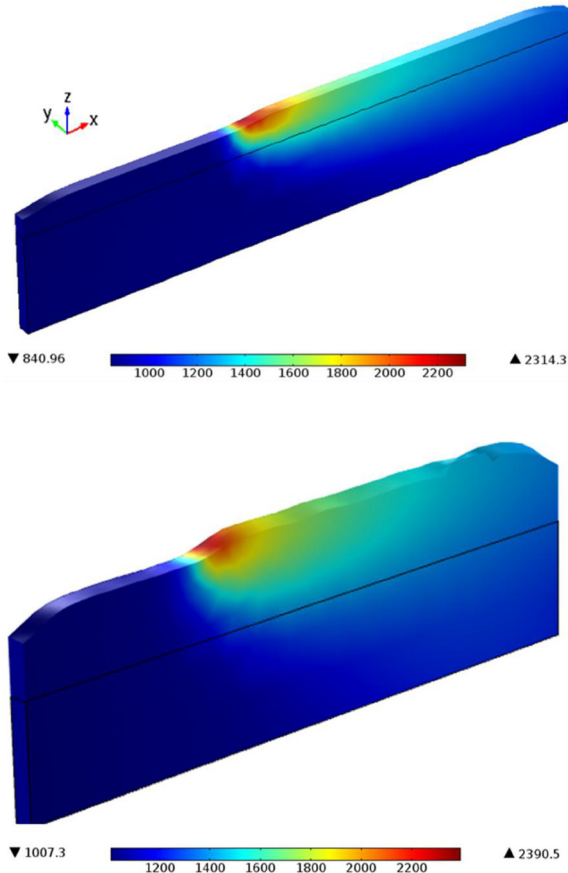


FIG. 6. 3D temperature fields calculated during the (a) 4th additive layer (P600 V400) and (b) 6th additive layer (P600 V200).

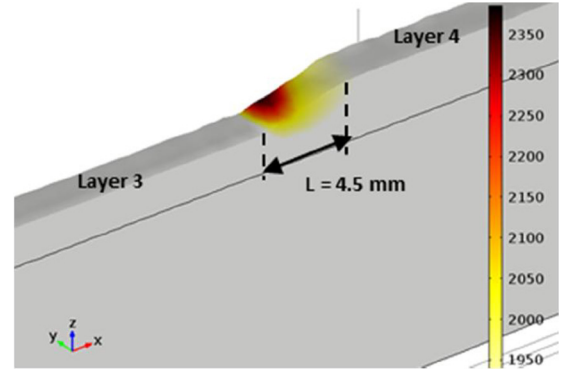


FIG. 7. Estimation of melt-pool dimensions (P600 V200).

III. RESULTS

The FE model provides us with the following data: (1) the geometry of manufactured layers (mainly layer height A_h and width e), (2) the melt-pool dimensions (H and L), (3) the 3D temperature fields and time history of all the constitutive nodes and positions (x,y,z) (Figs. 6 and 7). CPU times for a four-core computer with 16 Go RAM were approximately 45 min per additive layer, including laser scanning duration and time pause. Such a calculation time can be considered as rather short and should allow the calculation of much more complex and large parts using the same procedure.

Considering a constant laser power P_0 , an absorption coefficient of $A=0.28$ and two different scanning speeds, simulations and resulting 3D thermal fields (Fig. 6), indicate a clear difference in layer height, but a limited effect on MP maximum temperature and fusion isotherm (Fig. 7). Such an absorption coefficient is in the same order of magnitude (around 0.3) but a little higher than what has been previously found in anterior work.¹⁶

When compared with experimental data, it was confirmed that numerical results (Table II, Fig. 8), provided a correct estimation of layer heights and melt-pool dimensions (MP), despite a slight overestimation (+10%) of MP height and length by the numerical model as shown in the histograms of Fig. 8.

Moreover, MP maximum temperatures comprised between 2100 and 2400 K (Tables II and III) were estimated by the model.

Numerical thermal cycles $T=f(t)$ were also plotted versus thermocouple measurements carried out in the center part (Fig. 9) or the edge (Fig. 10) of the starting substrate. In both cases, and for P400V200 and P600V200 conditions, a satisfactory agreement is obtained even if 50–100 K temperature

TABLE II. Numerical calculations of LMD walls.

P400 V400	P400 V200	P600 V400	P600 V200
$P_0 = 400$ W	400 W	600 W	600 W
$V_s = 0.4$ m/min	0.2 m/min	0.4 m/min	0.2 m/min
$e = 2.1$ mm	2.5 mm	2.6 mm	3.3 mm
$\Delta h = 0.65$ mm	1.1 mm	0.57 mm	0.95 mm
$L = 3.4$ mm	4 mm	4.2 mm	4.5 mm
$H = 1.2$ mm	1.6 mm	1.3 mm	2 mm

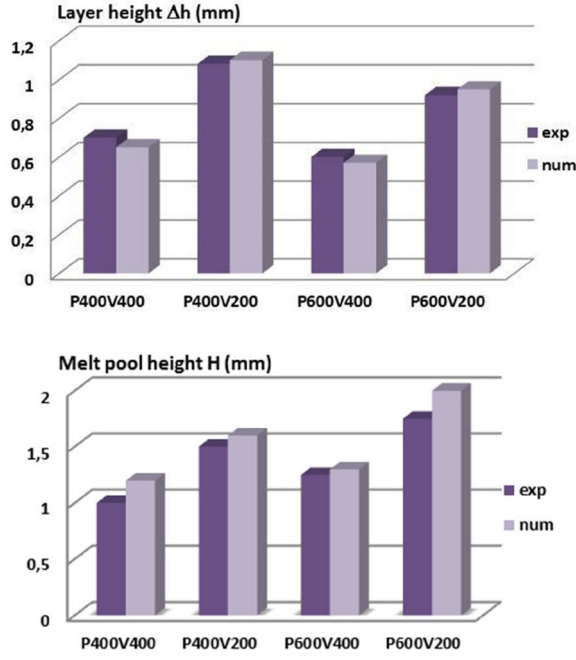


FIG. 8. Comparison between numerically simulated and experimental layer heights and melt-pool heights.

differences are shown in the very first recorded thermal cycle (Figs. 9 and 10). This confirms the global validity of the proposed thermomorphological calculation of LMD.

Compared with previously reported works, the model presented here has combined a realistic 3D description of layer addition, derived from the 2D approach by Morville *et al.*,¹¹ with a global experimental validation using dedicated diagnostics.

The global validation of thermal fields made possible the estimation of thermal gradients G (K/m), cooling rates V_c (K/s), and solidification front velocity R (m/s) (considered as equal to V_c/G) near the solidification front. Average data (edge and middle of the MP) were recorded for the four experimental conditions (V_c estimated in Fig. 11) and reported on a micro structure map established by Kobryn¹⁵ for Ti-6Al-4V alloy (Fig. 12) using a thermodynamical calculation of the columnar to equiaxed transition (CET) based upon Hunt criterion. Such a microstructure map indicates that columnar grains are usually obtained for large gradients and rather low solidification rates. From the numerical calculation, a columnar microstructure was predicted for all the LMD conditions, but at the limit of the columnar-to-mixed transition. Experimentally determined microstructures were

TABLE III. Numerical calculations of cooling rate, thermal gradient, and solidification conditions.

	V_c (K/s)	G (K/m)	R (m/s)	T_{max} (K)
P400 V400	720	4.2×10^5	0.0017	2130
P400V200	210	2.3×10^5	0.0009	2170
P600V400	410	3.2×10^5	0.0012	2330
P600V200	180	2.4×10^5	0.0007	2390

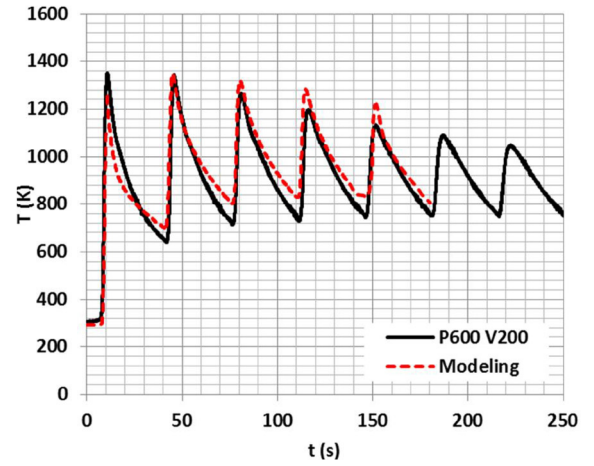
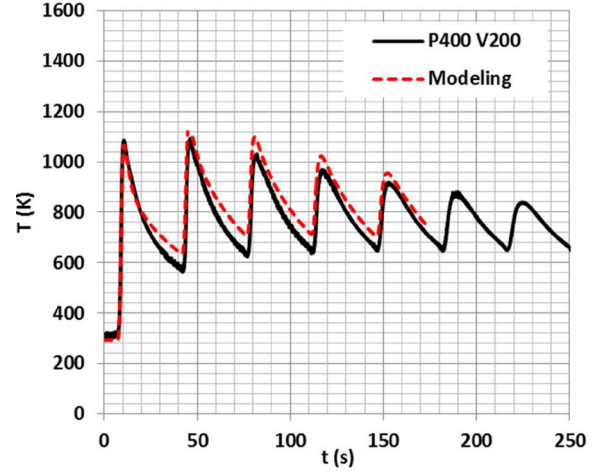


FIG. 9. Comparison of temperature profiles recorded by thermocouples (black) in the center part of the substrate at a location of ($x_0 = 31$ mm, $z_0 = -3$ mm) below the top surface and calculated by the FE model (dotted line, red): (a) P400 V200, (b) P600 V200.

found to be mostly columnar except for (P400 V400) condition (Fig. 13). The reason why a equiaxed microstructure could not be predicted by the model for (P400 V400) is not clear yet but could be due: (1) either to a bad numerical

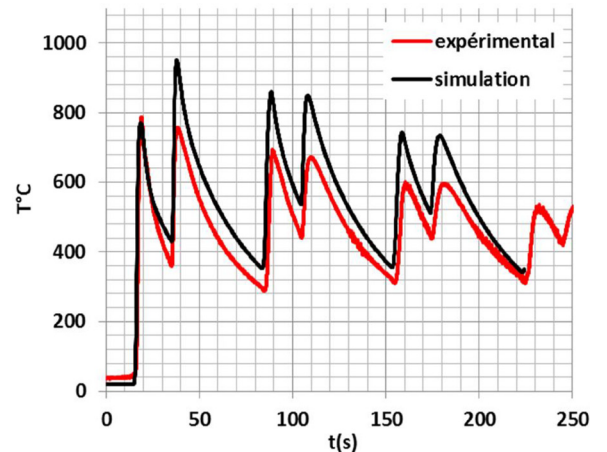


FIG. 10. Comparison of $T = f(t)$ profiles recorded by thermocouples (red) in the substrate at the edge of the wall substrate ($x_0 = 56$ mm, $z_0 = -3$ mm) and calculated by the FE model (black) (P400 V200).

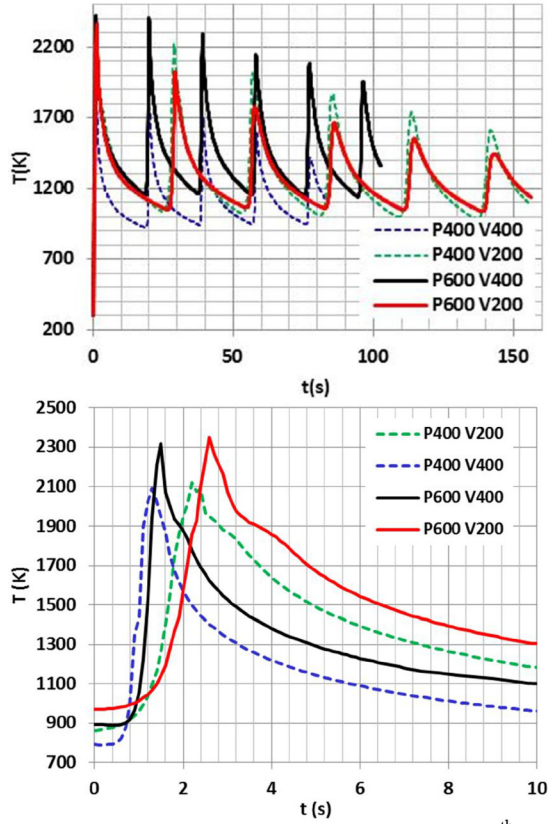


FIG. 11. $T=f(t)$ profiles calculated at the 4th LMD layer for the 4 experimental conditions: (a) time profile between layer 4 and layer 9, (b) zoom on the temperature profile during the 4th layer.

description of the interlayer dilution (for P400 V400, the dilution rate is low and favours noncolumnar grains), (2) or to the microstructure map established by Kobryn using the Hunt criterion¹⁵ itself which should not be predictive and generalized enough due to the adjustment of nucleation parameters or to the estimation of supercooling conditions used to determine the CET.

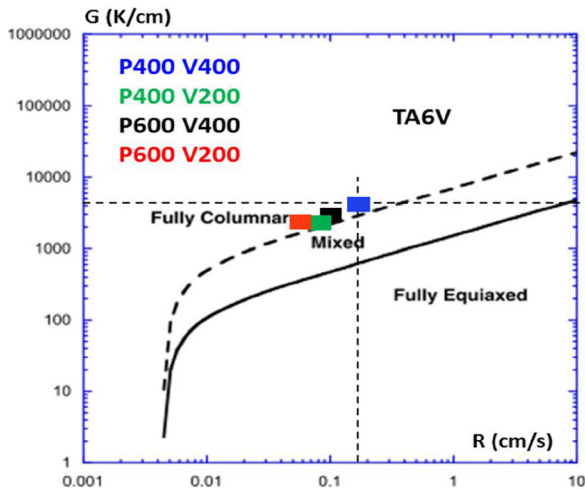


FIG. 12. Ti6Al4V microstructure map (Ref. 15) and prediction of grain microstructures.

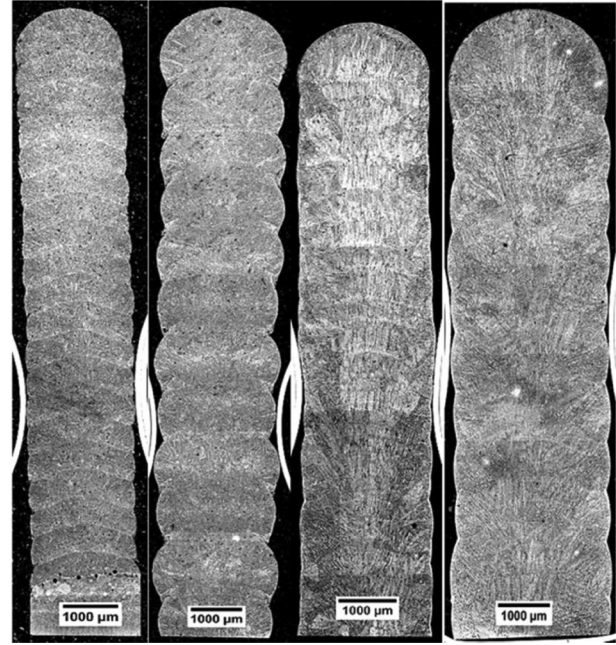


FIG. 13. Cross sections of LMD samples: (a) P400 V400 (equiaxed), (b) P400 V200 (mixed), (c) P600 V400 (columnar), and (d) P600 V200 (columnar).

IV. CONCLUSION

A simplified model for LMD has been developed, based on the ALE free surface motion of additive layer surfaces combined with realistic laser irradiation and boundary conditions, but without considering fluid flow to simplify calculation procedure. It allows determining the shape of manufactured walls and corresponding temperature fields in an affordable amount of time, with a better representation of MP shape than classical Lagrangian models. The thermal model has been validated by comparison with dedicated experimental data (melt-pool analysis, thermal measurements) on a Ti-6Al-4V alloy for up to ten additive layers. Last, the use of calculated thermal distributions behind the melt-pool was used in combination with microstructural maps to predict the grain structure of LMD walls. However, the microstructure map was not found to be predictive enough for all the LMD conditions, and for the Ti-6Al-4V powder used experimentally.

NOMENCLATURE

- A = absorption coefficient
- A_h = layer height (m)
- C_p = specific heat (J/kg/K)
- D_0 = laser diameter (m)
- D_m = mass feed rate (kg/s)
- D_{meff}^* = efficient mass feed surface rate (kg/s/m²)
- e = melt-pool and layer width (m)
- G = thermal gradient (K/m)
- H = melt-pool height (m)
- h_c = natural convection coefficient (= 15 W/m²/K)
- L = melt-pool length (m)
- L_m = latent heat of melting (J/kg)

P_0 = laser power (W)
 R = solidification front velocity (m/s)
 r_p = powder stream radius (m)
 r_0 = laser radius (m)
 T_m = melting temperature (K)
 T_{\max} = maximum temperature in the melt-pool (K)
 V_c = cooling rate (K/s)
 V_s = solidification rate (m/s)
 V_0 = laser scanning speed (m/s)
 ΔT = interval of solidification (K)
 $\lambda(T)$ = conductivity (W/m/K)
 ρ = density (kg/m³)
 O_0 = laser power density (W/m²)

¹Y. L. Huang, J. Liu, N. H. Ma, and J. G. Li, "Three-dimensional analytical model on laser-powder interaction during laser cladding," *J. Laser Appl.* **18**, 42–46 (2006).

²H. Qi, J. Mazumder, and H. Ki, "Numerical simulation of heat transfer and fluid flow in coaxial laser cladding process for direct metal deposition," *J. Appl. Phys.* **100**(2), 024903 (2006).

³S. Wen and Y. C. Shin, "Modeling of transport phenomena in direct laser deposition of metal matrix composites," *Int. J. Heat Mass Transfer* **54**, 5319–5326 (2011).

⁴S. Pouzet, P. Peyre, C. Gorny, O. Castelnaud, T. Baudin, and F. Brisset, "Direct metal deposition of titanium matrix composites using B₄C powder," in Proceedings of ICALCO Conference, Atlanta, GA, 17–22 October 2015.

⁵S. Gosh and J. Choi, "Modeling and experimental validation of stresses and microstructure formation in multi-layer laser-aided DMD process," *J. Heat Transfer* **128**, 662–679 (2006).

⁶R. Ye, J. E. Smugeresky, B. Zheng, Y. Zhou, and E. J. Lavernia, "Numerical modeling of the thermal behavior during the LENS process," *Mater. Sci. Eng. A* **428**, 47–53 (2006).

⁷A. Pinkerton and L. Li, "Modelling the geometry of a moving laser melt-pool and deposition track via energy and mass balances," *J. Phys. D: Appl. Phys.* **37**, 1885–1888 (2004).

⁸A. Fathi, E. Toyserkani, A. Khajepour, and M. Durali, "Prediction of melt-pool depth and dilution in laser powder deposition," *J. Phys. D: Appl. Phys.* **39**, 2613–2623 (2006).

⁹L. Han, K. M. Phatak, and F. W. Liu, "Modeling of laser deposition and repair process," *J. Laser Appl.* **17**(3), 89–99 (2005).

¹⁰S. M. Thompson, L. Bian, N. Shamsaei, and A. Yadollahi, "An overview of direct laser deposition for additive layer manufacturing, Part I: Transport phenomena, modeling and diagnostics," *Addit. Manuf.* **8**, 36–62 (2015).

¹¹S. Morville, M. Carin, P. Peyre, M. Gharbi, D. Carron, P. Le Masson, and R. Fabbro, "2D longitudinal modeling of heat transfer and fluid flow during multilayered DLMD process," *J. Laser Appl.* **24**(3), 032008 (2012).

¹²S. Morville, "Modélisation multiphysique du procédé de Fabrication Directe par Projection Laser en vue d'améliorer l'état de surface final," Ph.D. dissertation, University of South Brittany, France, 2012.

¹³F. K. Mirzade, V. G. Niziev, V. Y. Panchenko, M. D. Khomenko, R. V. Grishaev, S. Pityana, and C. Van Rooyen, "Kinetic approach in numerical modeling of melting and crystallization at laser cladding with powder injection," *Physica B* **423**, 69–76 (2013).

¹⁴A. Suarez, M. J. Tobat, A. Yanez, I. Perez, and J. J. Candel, "Modeling of phase transformations of Ti6Al4V during laser metal deposition," *Phys. Proc.* **12**, 666–673 (2011).

¹⁵P. Kobryn and S. L. Semiatin, "Microstructure and texture evolution during solidification processing of Ti-6Al-4V," *J. Mater. Process. Technol.* **135**, 330–339 (2003).

¹⁶P. Peyre, R. Neveu, P. Aubry, R. Fabbro, and A. Longuet, "Analytical and numerical modelling of the direct metal deposition laser process," *J. Phys. D: Appl. Phys.* **41**, 025403 (2008).

¹⁷M. Gharbi, P. Peyre, C. Gorny, R. Fabbro, M. Carin, S. Morville, D. Carron, and P. Le Masson, "Influence of various process conditions on surface finishes induced by the direct metal deposition laser technique on a Ti-6Al-4V alloy," *J. Mater. Process. Technol.* **213**, 791–800 (2013).